CrossMark

Time-temperature-precipitation and property diagrams for super duplex stainless steel weld metals

Vahid A Hosseini [1,2] · Leif Karlsson [1] · Dirk Engelberg [3] · Sten Wessman [1]

Abstract

Super duplex stainless steel (SDSS) weld metal microstructures, covering the complete temperature range from ambient to liquidus, were produced by arc heat treatment for 1 and 10 min. Temperature modeling and thermodynamic calculations complemented microstructural studies, hardness mapping and sensitization testing. After 1 min, intermetallics such as sigma and chi phase had precipitated, resulting in moderate sensitization at 720–840 °C. After 10 min, larger amounts of intermetallics resulted in hardness up to 400 HV0.5 and more severe sensitization at 580–920 °C. Coarse and fine secondary austenite precipitated at high and low temperatures, respectively: The finer secondary austenite was more detrimental to corrosion resistance due to its lower content of Cr, Mo, and N as predicted by thermodynamic calculations. Increased hardness and etching response suggest that 475 °C embrittlement had occurred after 10 min. Results are summarized as time-temperature-precipitation and property diagrams for hardness and sensitization.

1 Introduction

Super duplex stainless steels (SDSS), with a microstructure consisting of approximately equal amounts of ferrite and austenite, present an excellent combination of toughness and

The original version of this article was revised: Tables 4-6 have been displayed erroneously.

Recommended for publication by Commission IX - Behaviour of Metals Subjected to Welding

✉ Vahid A Hosseini
vahid.hosseini@hv.se

Leif Karlsson
leif.karlsson@hv.se

Dirk Engelberg
d.engelberg@manchester.ac.uk

Sten Wessman
sten.wessman@hv.se

[1] Department of Engineering Science, University West, SE-461 86 Trollhättan, Sweden

[2] Innovatum AB.,Trollhättan, SE-461 29 Trollhättan, Sweden

[3] School of Materials, The University of Manchester, Manchester M13 9PL, UK

corrosion resistance [1–4]. However, a large imbalance in ferrite/austenite ratio and/or the precipitation of unwanted secondary phases such as nitrides, intermetallics, and sometimes secondary austenite may result in the degradation of properties [5, 6]. This is typically due to excessive heating and reheating during fabrication and processing, such as cutting, heat treatment, and welding [7]. To avoid the formation of nitrides and an unacceptably high ferrite content during welding, filler metals overalloyed in Ni, shielding and backing gases with N-additions, and/or higher heat input are recommended to promote austenite formation [8]. However, in thicker structures and multipass welding [8], the heat input has to be balanced against the fact that sigma phase can precipitate quickly at 600–1000 °C [4, 9]. The precipitation of secondary austenite, furthermore, is a well-known phenomenon occurring in multipass welds often leading to a reduction of corrosion resistance [6, 10]. Knowledge about allowable combinations of times, temperatures, and cooling and heating rates to avoid detrimental changes of the microstructure is therefore essential for efficient fabrication and processing.

Some information about the influence of heat treatment temperature and time on the microstructure of SDSS weld metal is available but is far from complete. Nishimoto et al. [9] studied sigma phase precipitation in a 2507 weld metal, but the chemical composition (lower

Ni) and high ferrite content (78%) were different compared to the standard requirement and practice. This therefore could produce unrealistic results for predication of phase transformation in real welding. Nilsson et al. [11] investigated the precipitation of secondary phases in different SDSS weld metals, for a selection of times and temperatures. Hosseini et al. [12, 13] performed multipass TIG remelting to study the precipitation of sigma phase in the heat-affected zone of a wrought SDSS alloy; however, the weld metal was not studied and the thermal cycles did not allow for studies of effects of longer heat treatments. In particular, the precipitation temperature and morphology of deleterious secondary phases need further research. The obvious reason for the lack of information is the time and effort required to make the comprehensive microstructural studies required to produce time-temperature-precipitation (TTP) or continuous cooling transformation (CCT) diagrams. Conventional heat treatment practices [14, 15] and physical simulators such as the Gleeble thermomechanical tester [16] and TIG remelting [13] can be employed to study the influence of thermal cycles on the microstructure and properties. However, these methods are time-consuming when used to cover a large range of times and temperatures. Hosseini et al. [17] recently introduced a novel heat treatment technique where a stationary TIG arc is applied on a disk-shape specimen. This method makes it possible to cover the full range of temperatures from room temperature to liquidus in a single specimen, thereby greatly reducing the number of samples needed and also the characterization time required.

This study aims at complementing current knowledge by characterizing the microstructure, sensitization behavior, and hardness of a SDSS weld metal, for all temperatures from ambient to liquidus, after heat treatment for 1 and 10 min. Functionally graded microstructures covering the complete temperature range were produced by arc heat treatment of as-welded SDSS weld metal, and local temperatures were determined by temperature field modeling calibrated by measurements. Evaluation of microstructures was complemented by thermodynamical calculations. Results are summarized as TTP and property diagrams.

2 Experimental

2.1 Materials and welding

A schematic illustration of the procedure used for producing weld metal specimens for arc heat treatment is shown in Fig. 1. An 8 × 30-mm rectangular groove in a 20-mm-thick type 2507 SDSS plate was filled with 25

TIG welding passes using 2509 type welding filler material and Ar-30%He-2%N_2 shielding gas. The procedure ensured a minimum dilution with base material in the weld metal. The chemical compositions of the base and filler materials are presented in Table 1.

As the next step, a plate with the dimensions of 200 × 100 × 6 mm was machined from the plate, with the weld metal located in the center. An autogenous TIG remelting pass was applied along the weld centerline using Ar-2%N_2 shielding gas, where the welding current, voltage, and speed were 145 A, 14.5 V, and 1.6 mm/s, respectively. The aim was to homogenize the chemical composition and microstructure of the weld metal to be studied. A cross section of the plate with as-welded and remelted regions can be seen in Fig. 1. Finally, two 99-mm-diameter disks for arc heat treatment were waterjet cut from the plate.
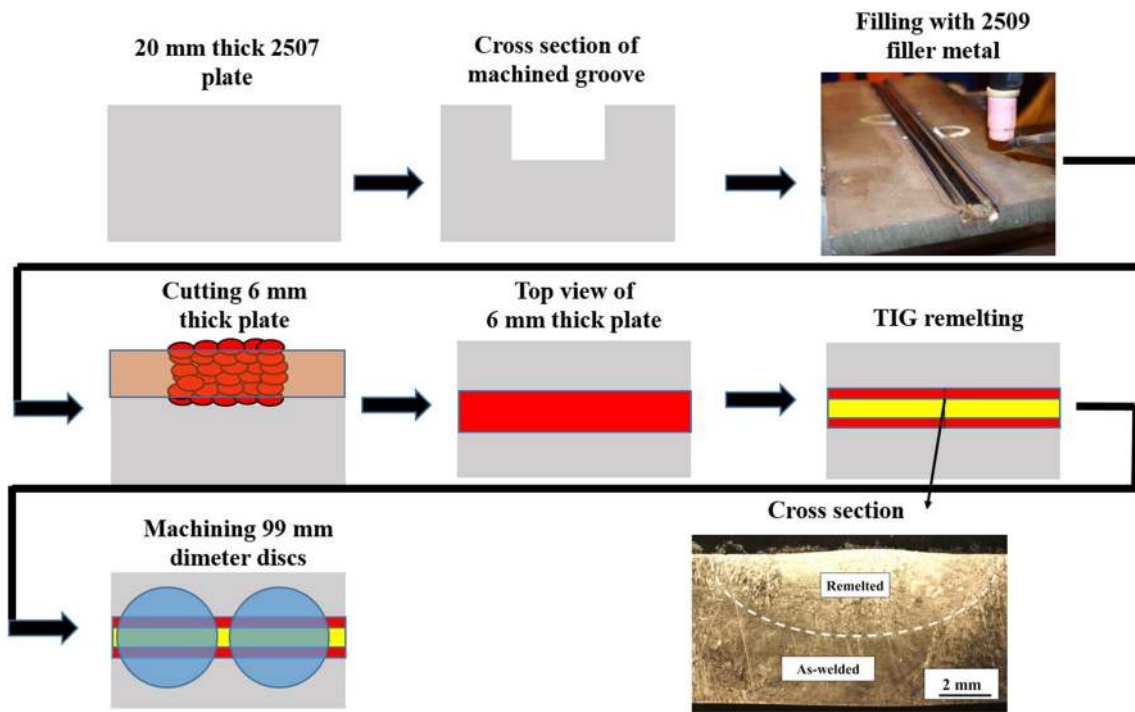
2.2 Arc heat treatment

A top view of the arc heat treatment device and a schematic illustration of the equipment are shown in Fig. 2. The disk-shaped sample, produced as explained in Sect. 2.1, was mounted on the water cooled chamber, and a stationary TIG arc was applied. An arc current of 100 A and an arc length of 3 mm were used to heat treat two samples for 1 and 10 min, respectively. More details about the arc heat treatment technique can be found in [17].

In addition, thermal cycle analysis was performed on 2507 SDSS base material by attaching several thermocouples, as shown in Fig. 2a. Data from the thermal cycle analyses was employed to calibrate a model giving the steady-state temperature distribution in the sample during arc heat treatment as described in Sect. 2.4.

2.3 Characterization techniques

Cross sections from arc heat-treated samples were prepared by waterjet cutting, grinding, and polishing employing standard procedures. Samples were studied after electrolytical etching with 10 wt.% NaOH for 4 s with 4 V and after etching with a modified Beraha's etchant using an Olympus BX60M microscope. Polished samples were also studied using the back scattered electron mode (BSE) in a Toshiba TM3000 scanning electron microscope (SEM). In duplex stainless steels and weld metals, intermetallics such as sigma and chi are easily recognizable using atomic number contrast in BSE SEM. This technique was therefore employed to measure the sigma phase content and to detect the precipitation of chi phase.

Electron back-scattered diffraction (EBSD) analysis was also performed to identify phases. A colloidal silica polished sample was used for EBSD to provide the maximum indexing rate. A Zeiss Sigma HDVP interfaced

Fig. 1 Illustration of procedure for preparation of disk-shaped samples for arc heat treatment. A groove was machined and filled with 2509 SDSS filler material. A TIG remelting pass (yellow) was applied to homogenize the weld metal. Finally, two samples were extracted with the TIG remelted pass at the center

with a Nordlys EBSD detector from Oxford Instruments was employed for EBSD analysis using a step size of 110 nm and an accelerating voltage of 20 kV. The Aztec 2.1 and HKL Channel 5 software packages were used for data acquisition and analysis, respectively.

Ferrite numbers were measured from the arc heat treatment fusion zone to 5 mm from the fusion boundary using a Fischer Feritscope.

A Struers DuraScan 80 automated hardness tester was utilized to map the microhardness of heat-treated samples using a 500-g load. The number of indents were 274 and 685 for the samples arc heat treated 1 and 10 min, respectively. The procedure of hardness mapping is explained by Brayshaw et al. [18].

The sensitization of duplex stainless steels is due to the low Cr and Mo contents in regions adjacent to intermetallics and nitrides and also sometimes the formation of secondary austenite with low Cr and N [12]. Sensitization testing was performed based on ASTM A262 [19], Practice A with some modification. Samples were electrolytically etched in 10 wt.% oxalic acid for 1 min with an applied voltage of 2 V. The degree of sensitization and location of sensitized regions were evaluated by light optical microscopy.

2.4 Temperature field modeling and thermodynamic calculations

The steady-state temperature distribution around the fusion zone has previously been modeled using the open source computational software OpenFOAM® [17, 20]. The existing model was used but adapted to the actual geometries of the fusion zones in the 1- and 10-min arc heat-treated samples. Temperature measurements used for calibration had previously been performed on 2507 base material, as explained in Sect. 2.2. Figure 3 shows that the thermal properties of the 2507 type base material and the 2509 type filler material are nearly identical
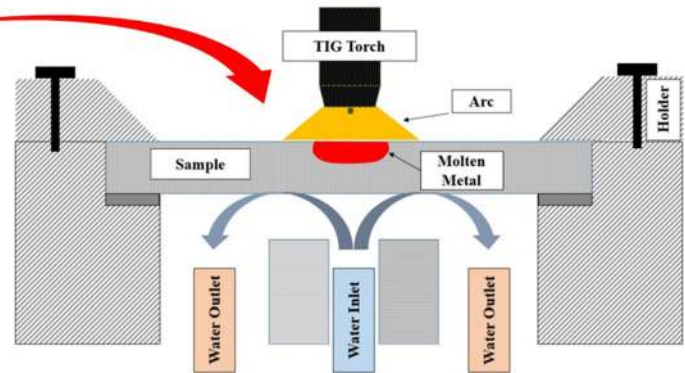
Table 1 Chemical composition (wt.%) of 2507 type base and 2509 filler material

	C	Si	Mn	P	S	Cr	Ni	Mo	N	Cu	W	Fe
Base metal	0.016	0.44	0.76	0.028	0.001	25.04	6.93	3.78	0.265	0.40	–	Bal.
Filler metal	0.015	0.40	0.61	0.014	0.001	25.53	9.22	4.04	0.260	0.09	0.04	Bal.
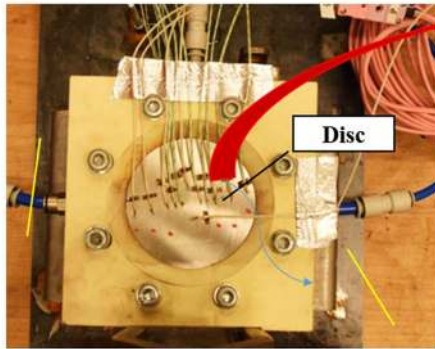
Fig. 2 Arc heat treatment. **a** Attachment of thermocouples (TC) on the top side of the disc shaped sample. **b** Schematic illustration of the arc heat treatment device with a stationary TIG arc on the top side and water cooling on the back side producing a steady-state condition

why the existing model [17] could be applied to the weld metal samples.

Equilibrium phase fractions and TTP diagrams were calculated using JMatPro, version 6.2.1, for the actual chemical composition of the filler material (Table 1).

3 Results

3.1 Macrostructure and temperature distribution

A schematic illustration of the cross section of an arc heat treatment sample (see Fig. 1 for procedure of preparation) is shown in Fig. 4a. As welded and remelted regions and the arc heat treatment fusion zone are shown.

Cross sections and corresponding steady-state temperature distribution maps, produced by modeling, for 1 and 10 min arc heat-treated samples are shown in Fig. 4b, c.

The fusion zone is fully ferritic in both samples whereas a graded microstructure, as revealed by variations in the etching response, was formed in the region heat affected by the arc heat treatment.

1The temperature profiles are very similar for the two samples with the main difference being the slightly larger weld pool for the 10-min sample. In both cases, the temperature dropped to 600 °C within 2 mm from the FB showing the sharp temperature gradient next to the fusion boundary.

3.2 Calculated equilibrium phase and TTP diagrams

The equilibrium phase fraction diagram calculated by JMatPro for the 2509 filler material composition given in Table 1 is shown in Fig. 5a. The maximum stability temperature for sigma phase is 1070 °C, and the largest content is predicted to form at 600–800 °C. In addition to sigma phase, the precipitation of chi phase, G phase,

Fig. 3 Specific heat and thermal conductivity calculated by JMatPro for base (2507) and filler (2509) material with compositions as specified in Table 1
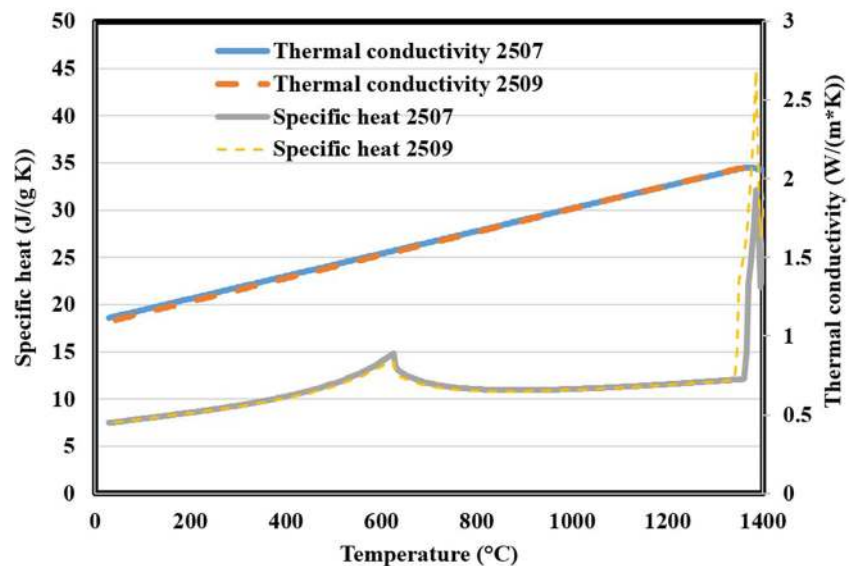
Fig. 4 **a** Schematic illustration of the regions in arc heat-treated samples showing the as-welded region, remaining from the filling of the groove, and the TIG remelted region with the fused zone from the arc heat treatment. Cross sections and temperature distribution maps of **b** 1 min and **c** 10 min arc heat-treated samples. The fusion zone is fully ferritic in both samples. Note the lower contrast between ferrite and austenite at locations corresponding to temperatures of about 475 °C in the 10 min sample
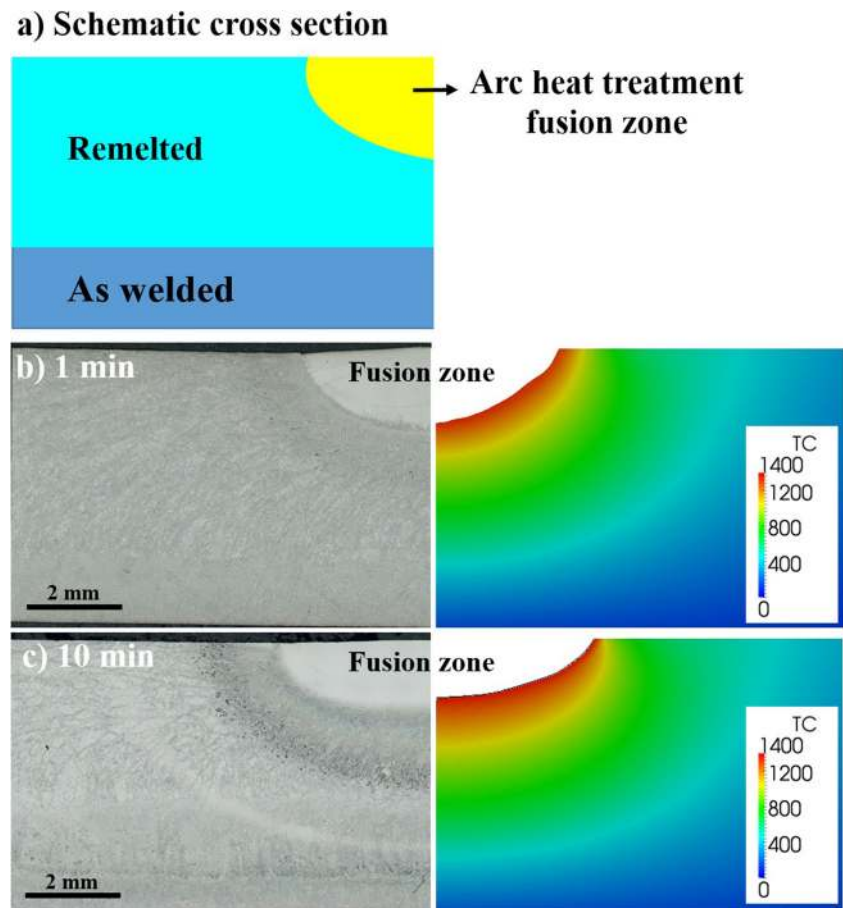
Laves, carbides, and nitrides is also predicted. Calculations also predict the formation of Cr-rich and Fe-rich ferrite below 500 °C known as 475 °C embrittlement.

TTP curves for 1 wt.% chi, 1 wt.% sigma, and 10 wt.% sigma in 2509 weld metal and 1 wt.% sigma in 2507 base material calculated by JMatPro are shown in Fig. 5b. The nose of the curves is at about 980 °C for 1 and 10% sigma phase in 2509 weld metal, but at 950 °C for 1% sigma phase in 2507 base material. The nose for 1% chi is located at 920 °C in 2509 weld metal.

3.3 Microstructure and hardness before arc heat treatment

Representative micrographs showing the microstructure of the as-welded and TIG-remelted weld metal, before the arc heat treatment, are presented in Fig. 6. The microstructure, in both regions, consists of a ferritic matrix with grain boundary and Widmanstätten austenite. Nitrides are also present inside the ferrite grains in the remelted microstructure. The ferrite numbers of as-welded and remelted regions were 37 ± 1 FN and 50 ± 1 FN, respectively. Microhardness mapping showed that

hardness was uniform in both regions varying between 260 HV0.5 and 290 HV0.5.

3.4 Microstructure of arc heat treated samples

In this section, the evolution of different microstructural constituents after 1 and 10 min arc heat treatment are presented.

3.4.1 Austenite and ferrite

The arc heat treatment fusion zone was fully ferritic in both the 1 and 10 min samples. The ferrite number was between 40 FN and 50 FN in the 1 min sample in the area next to fusion boundary of the arc heat treatment fusion zone (FB). In the 10 min sample, as shown in Fig. 7, the ferrite number was 75–96 FN next to the FB and then decreased to 30 FN 2 mm away before increasing to about 50 FN 5.5 mm from the FB. The complex, and in many regions very fine, microstructures of the arc heat-treated samples made ferrite content measurements by image analysis of optical micrographs impracticable and unreliable and was therefore not applied.

In the fusion boundary zone (FBZ), next to the fusion zone, the austenite is dissolving and gets finer with time as illustrated in Fig. 8a, b. This zone is a representative of the high-

Fig. 5 **a** Equilibrium phase fraction diagram for 2509 filler material. Secondary phases, such as sigma, chi, and nitrides, are predicted to form below about 1100 °C. **b** TTP diagrams calculated by JMatPro for 1% chi and sigma and 10% sigma in 2509 weld metal and 1% sigma in 2507 base material
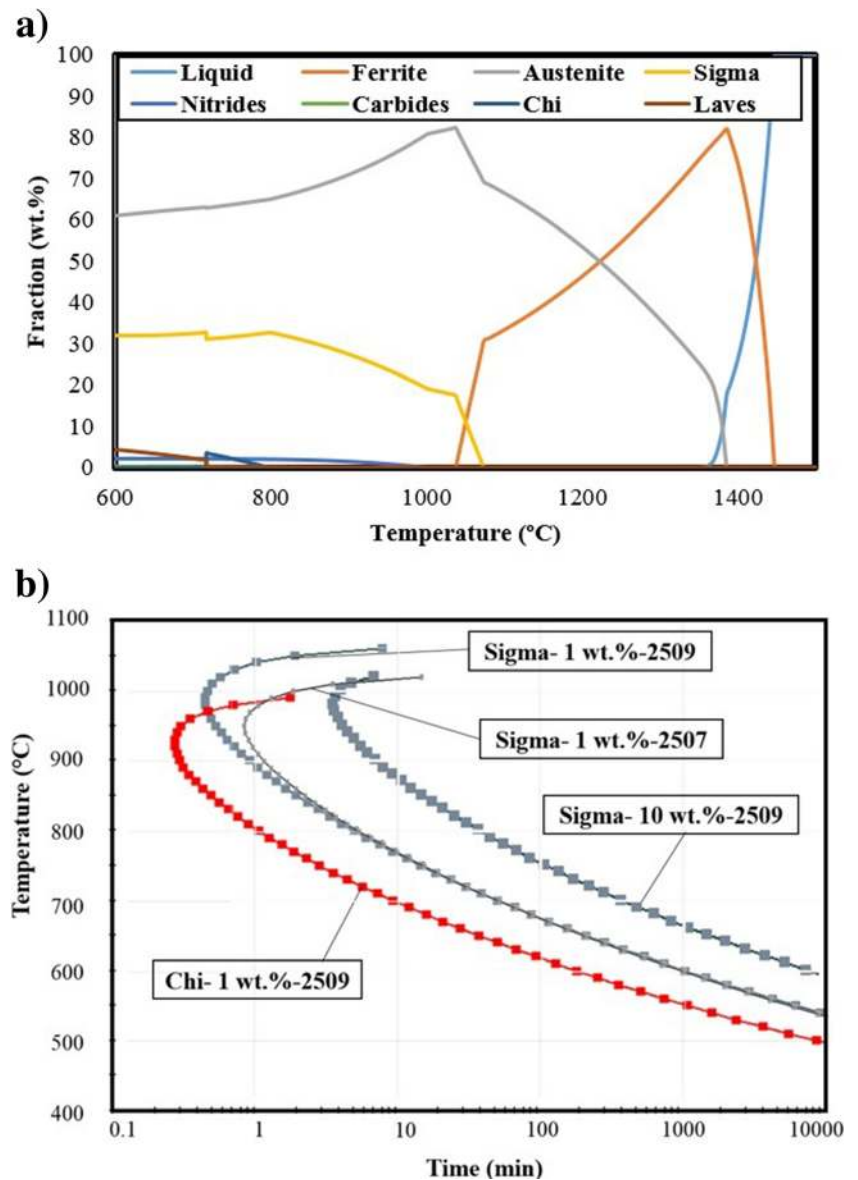

temperature heat-affected zone (HTHAZ) in duplex stainless steels. However, at the somewhat lower temperature of 1220 °C, the austenite content increases with heat treatment time (Fig. 8c, d) as the austenite coarsens.

3.4.2 Secondary phases

The highest temperatures where secondary austenite was observed was 960 °C after 1 min and 1110 °C after 10 min

Fig. 6 Microstructure of **a** the as-welded region and **b** the TIG remelted region before arc heat treatment
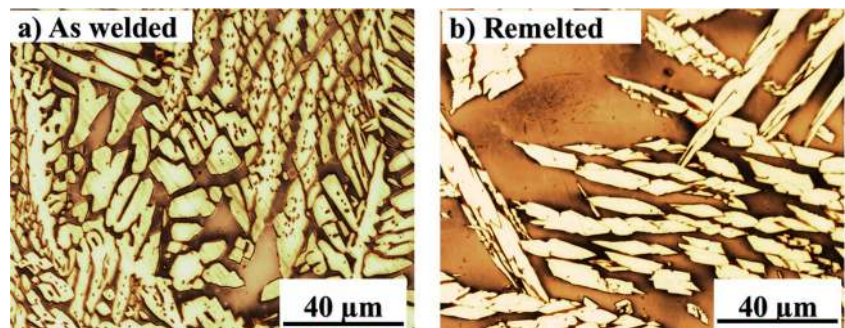
Fig. 7 Ferrite numbers in the vicinity of the FB in the 10 min sample. The ferrite number was 96 FN next to the FB, then decreased to 30–36 FN and reached the level of the unaffected remelted region about 5.5 mm from the FB
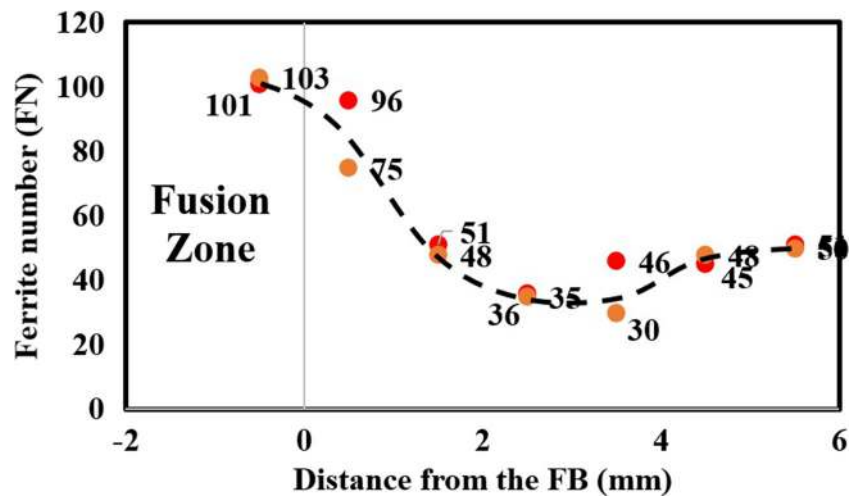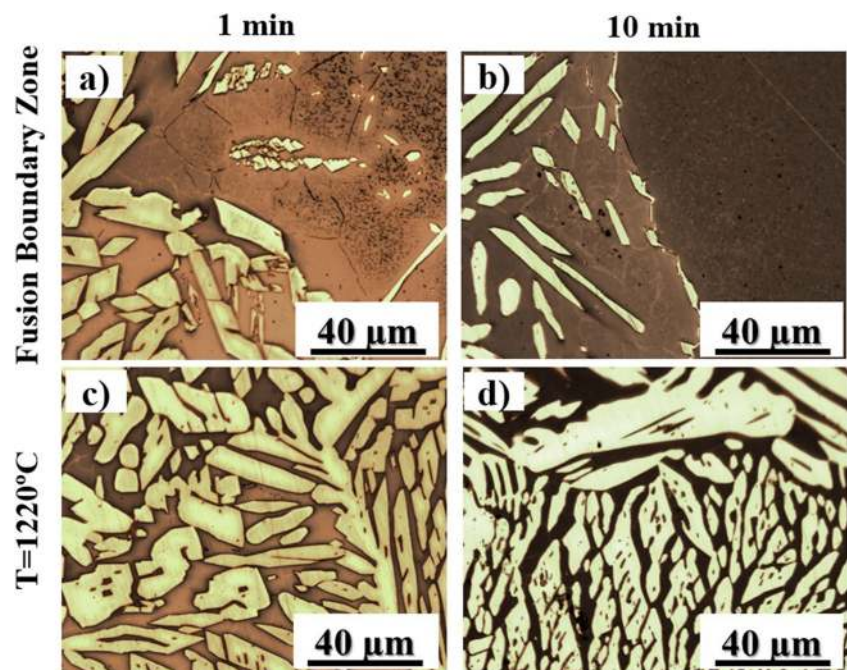

(Fig. 9). The secondary austenite was finer at lower temperatures and the content increased with heat treatment time. Table 2 shows that the range of secondary austenite formation temperature is wider for longer heat treatment time as the upper temperature limit goes up at the same time as the lower temperature limit decreases.

Representative BSE SEM micrographs of the 1 and 10 min samples for different temperatures are presented in Fig. 10. The bright gray phase is interpreted as sigma and the brightest particles as chi based on the expected typical compositions of these phases resulting in a brighter atomic contrast compared to ferrite and austenite. The highest temperature where traces of sigma phase were seen was 900 °C for the 1 min sample

and 1020 °C for the 10 min sample. As shown in Fig. 10, sigma was found as thick films in ferrite/austenite phase boundaries especially in narrow ferrite regions after 1 min heat treatment. In the 10 min sample, sigma had a more blocky shape at higher temperatures (with some cracks, Fig. 10b) and a combination of blocky and more coral like shapes at lower temperatures (Fig. 10d, f). The shape gradually changes from blocky to coral like with time as sigma grows as illustrated for 780 °C in Fig. 10e, f.

A typical BSE SEM micrograph and high-resolution EBSD phase maps from a location heat treated 10 min at about 850 °C are shown in Fig. 11. The microstructure consists of ferrite and austenite as well as sigma

Fig. 8 FBZ microstructure in **a** 1 min and **b** 10 min samples, showing austenite dissolution with increasing holding time. Some nitrides (dark spots) can be seen in the microstructure for both heat treatment times. Microstructure of regions heat treated at 1220 °C for **c** 1 min and **d** 10 min suggest coarsening of austenite

Fig. 9 Intragranular secondary austenite forming after arc heat treatment for 1 and 10 min. Coarser secondary austenite forms at higher temperatures (**a**, **b**) and finer at lower temperatures (**c**, **d**). The amount increase with longer holding time (**c**, **d**)
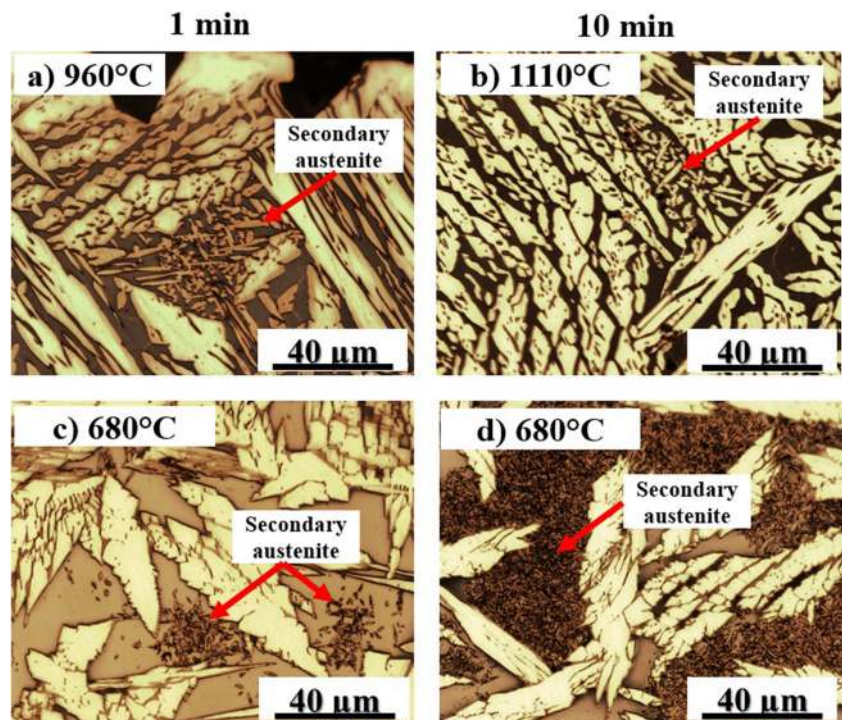
and chi phase. The content of sigma phase is much higher than chi. Sigma phase was typically found precipitating in narrow ferrite regions and among secondary austenite as shown in Fig. 11b, c, respectively.

The calculated equilibrium and measured contents of sigma phase are shown in Fig. 12 for the samples heat treated for 1 and 10 min. Sigma phase was not distributed uniformly in the microstructure which is why there was a large scatter in the measured content. The content and precipitation temperature range of sigma phase increased with increasing heat treatment time. However, the maximum content of sigma phase was observed at 780 °C for both heat treatment times with $3.3 \pm 0.6\%$ after 1 min and $18.0 \pm 6.0\%$ after 10 min. As expected the content of sigma phase is far from the equilibrium content calculated by JMatPro even after the 10 min heat treatment.

Chi phase is the brightest imaging phase in BSE SEM micrographs in Fig. 10 due to its high Mo content. Chi was

Table 2 Summary of temperature ranges for microstructural features and properties in arc heat-treated samples

Observation	1 min	10 min
Secondary austenite	640–960 °C	600–1110 °C
Sigma	720–900 °C	700–1020 °C
Chi phase	720–800 °C	650–940 °C
Sensitization	720–840 °C, FB	580–920 °C, FB
Hardness peaks	800 °C	700–920 °C, 450–480 °C

observed in ferrite/austenite boundaries as well as austenite/sigma phase boundaries. Chi phase was also found between secondary austenite grains, as shown in Fig. 11b. It formed discrete particles at high temperatures and thin films at ferrite/austenite boundaries at lower temperatures. In the 10 min sample, it covered a larger fraction of phase boundaries at lower temperatures.

Nitrides were observed in the FBZ (or HTHAZ) after 1- and 10-min aging as shown in Fig. 8a, b. They precipitated inside ferrite grains and the content decreased with increasing heat treatment time and decreasing temperature. It should be noted that these most likely formed on cooling after heat treatment rather than during the arc heat treatment.

3.5 Hardness

Microhardness maps of the 1 and 10 min samples are shown in Fig. 13. The fusion zone (formed due to remelting during arc heat treatment) showed higher hardness compared to the TIG remelted weld metal before arc heat treatment. After 1-min aging, the average hardness tended to be slightly increased in the region heat treated at around 800 °C. After 10-min aging, on the other hand, two regions with a higher hardness were observed as shown in Fig. 13. These regions were located around 800 and 475 °C with maximum hardness values of 400 HV0.5 and 320 HV0.5, respectively. It can be noted that the location of the band with low contrast between ferrite and austenite in Fig. 4 coincides with that of the second hardness band in Fig. 13.

Fig. 10 BSE SEM micrographs showing microstructure of 1 and 10 min arc heat-treated samples at different temperatures. The contents of sigma (gray) and chi (bright) phase increased with time. Sigma phase has a blocky shape at lower temperatures and a more coral-like morphology at higher temperature in the 10 min sample
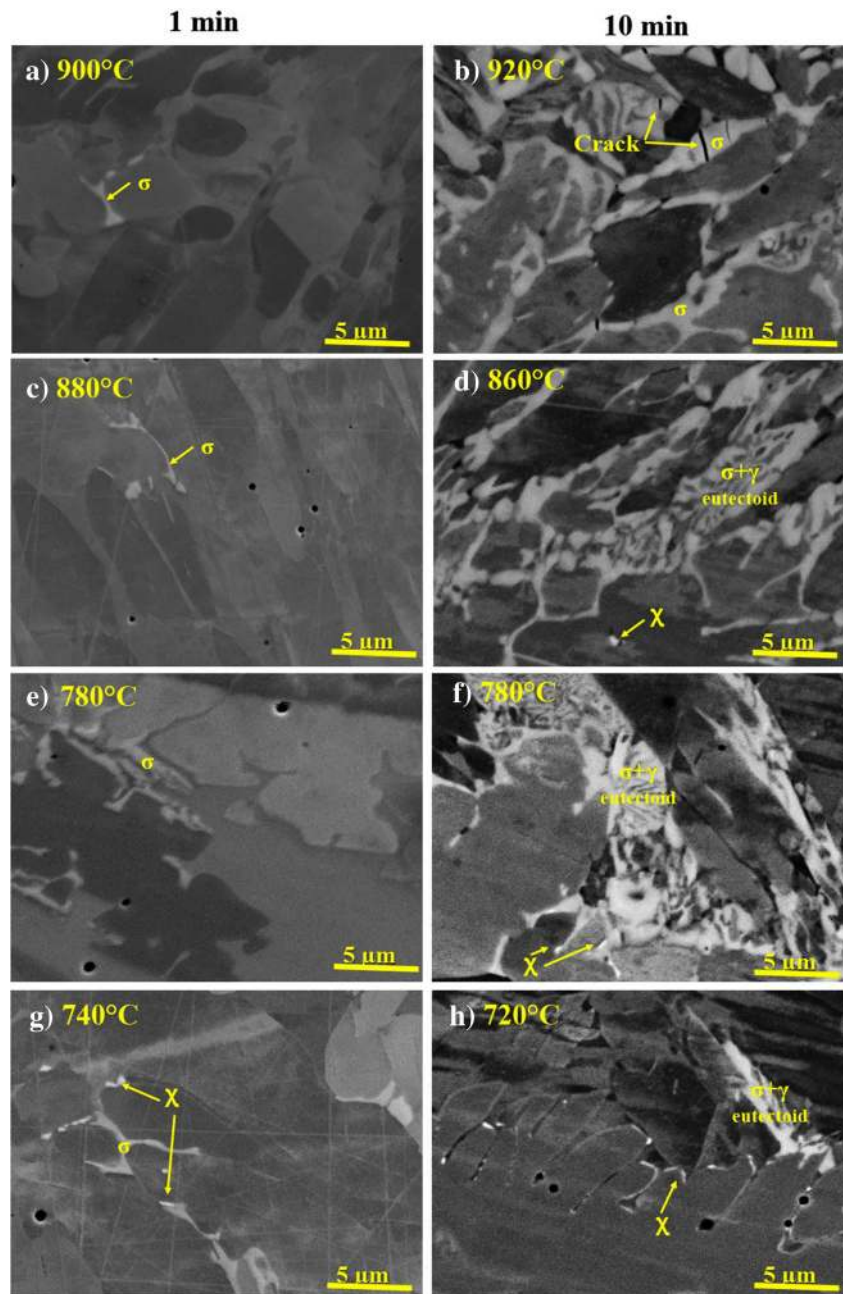

3.6 Sensitization

Light optical micrographs of 1 and 10 min samples after sensitization testing are presented in Fig. 14. The FBZ was sensitized where nitrides precipitated for both heat treatment times. The coarse secondary austenite formed at higher temperatures did not cause significant sensitization (Fig. 14b), but the finer forming at lower temperature (Fig. 14c) did. Narrow ferrite arms among primary austenite grains were sensitized after 1 min at 780 °C (Fig. 14d). After 10 min at the same temperature, the sensitization became much more pronounced as shown in Fig. 14f. Ferrite/austenite phase boundaries were also often sensitized after 10 min at 580 °C.

4 Discussion

The arc heat treatment technique produced a temperature gradient similar to that expected for welding, resulting in a graded microstructure. This section discusses how the microstructure evolves with time at different temperatures and how properties are affected.
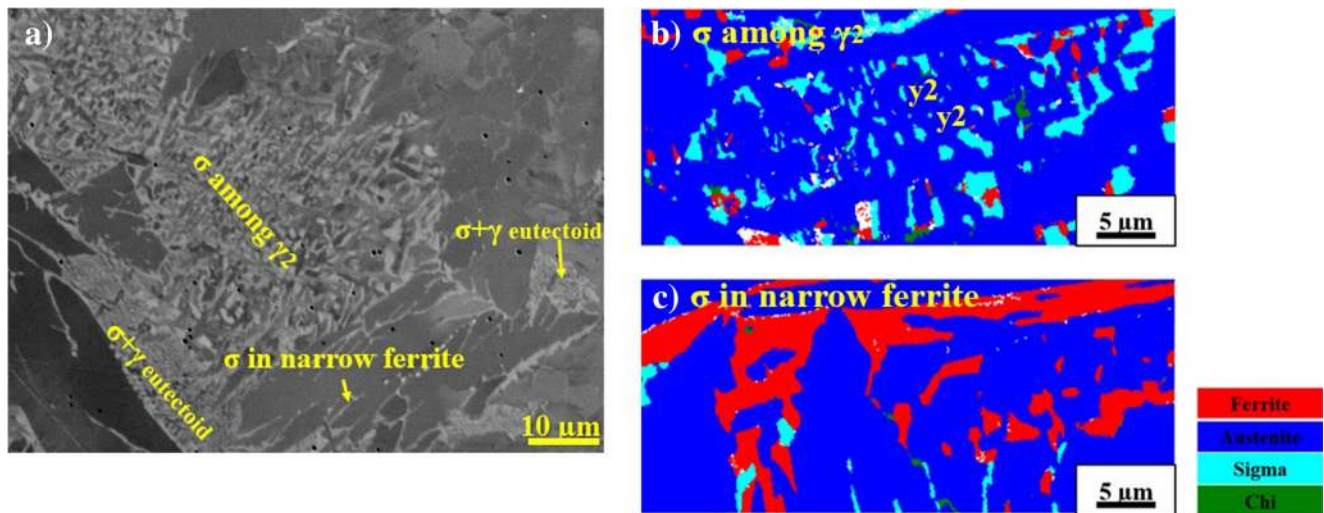
Fig. 11 **a** A typical BSE SEM microgaph of 10 min sample showing different locations where sigma phase precipitated at 850 °C. **b**, **c** EBSD phase maps from regions arc heat treated at 850 °C for 10 min. Sigma, chi, ferrite, and austenite are present in the microstructure

4.1 Overall changes in the microstructure

Schematic illustrations of the main phases of the weld metal, their morphology, and phase fractions after 1- and 10-min arc heat treatment are shown in Fig. 15. Changes, compared to the as-welded condition, are as expected more pronounced for longer heat treatment times as the equilibrium conditions are approached (Fig. 5). The remelted weld metal was markedly affected in a wide range of temperatures in the 10 min sample. For instance, only a few sigma phase particles were present at 800 °C, but significant amounts of sigma phase and secondary austenite were present after 10 min.

4.2 Ferrite/austenite

The austenite content decreased markedly above about 1250 °C (Fig. 8), HTHAZ, as the relative stability of the ferrite increased (Fig. 5) and due to nitrogen loss. After 10 min the

ferrite number was as high as 96 FN in the HTHAZ compared to 50 FN in unaffected remelted weld metal. Around 800 °C (Fig. 7), there was instead a reduction in ferrite number of 20 FN due to the transformation of ferrite to secondary phases, such as secondary austenite and sigma and chi phase.

It should be noted that the fully ferritic regions formed after 1- and 10-min arc heat treatments do not reflect real welding conditions due to the long time spent in the liquid state. However, it clearly shows the influence of nitrogen depletion on the microstructure.

4.3 Secondary phases

4.3.1 Secondary austenite

The driving force for precipitation of austenite, which is related to the difference between the initial and equilibrium austenite contents, increased with decreasing temperature. The austenite

Fig. 12 Measured and calculated equilibrium sigma phase content in 1 and 10 min arc heat-treated samples. The maximum content of sigma phase precipitated at 780 °C for both heat treatment times
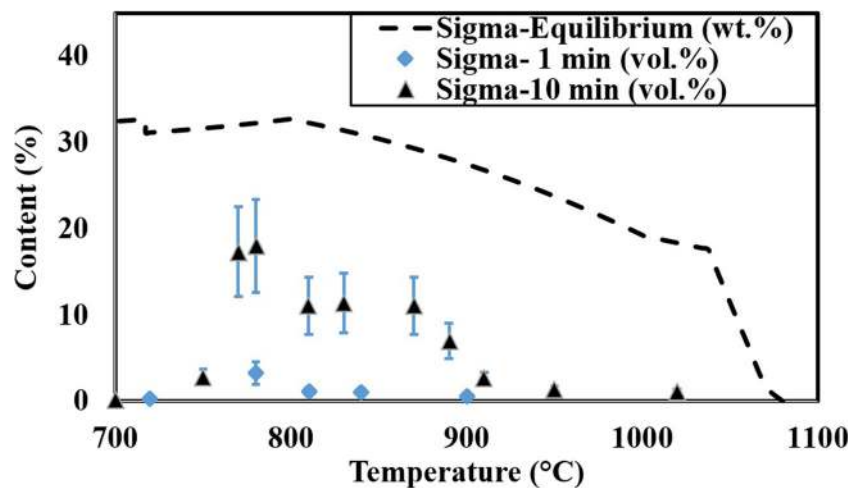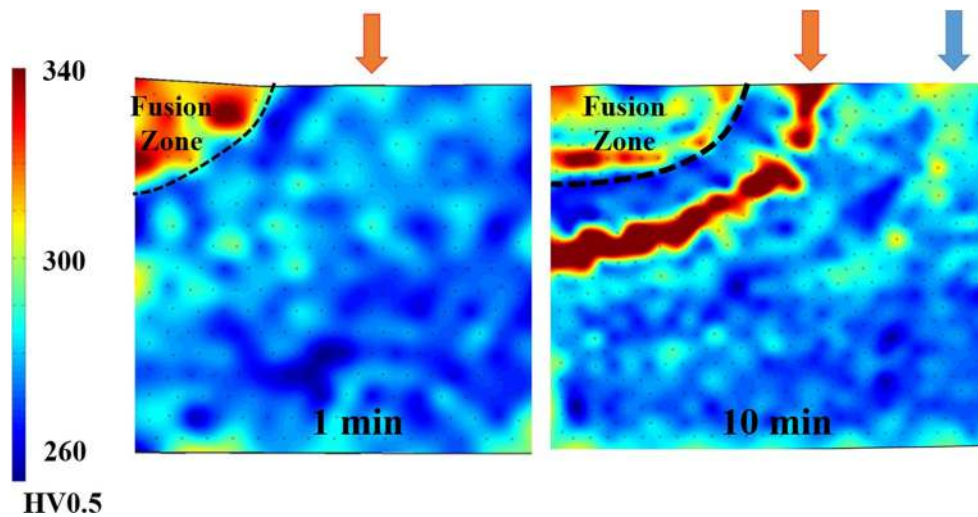
Fig. 13 Microhardness maps of samples arc heat treated for 1 and 10 min. The fusion zones are harder than before arc heat treatment. In the heat-affected region, hardness increased slightly in regions heat treated at around 800 °C in the 1 min sample (arrow). The same region shows very high hardness after 10-min heat treatment. Another high hardness region was found corresponding to heat treating at about 475 °C in the same sample

content increased during heat treatment by growth of primary austenite and precipitation of secondary austenite between approximately 600 and 1250 °C. A wider secondary austenite precipitation temperature range after 10 min compared to after 1 min (Table 2) is an indication of transformation through nucleation and growth [21]. It has been reported that secondary austenite mostly precipitates between 800 and 1000 °C; however, it has been seen at lower temperatures down to 600 °C [10, 21], which is in good agreement with the present observations. Finer secondary austenite, observed at lower
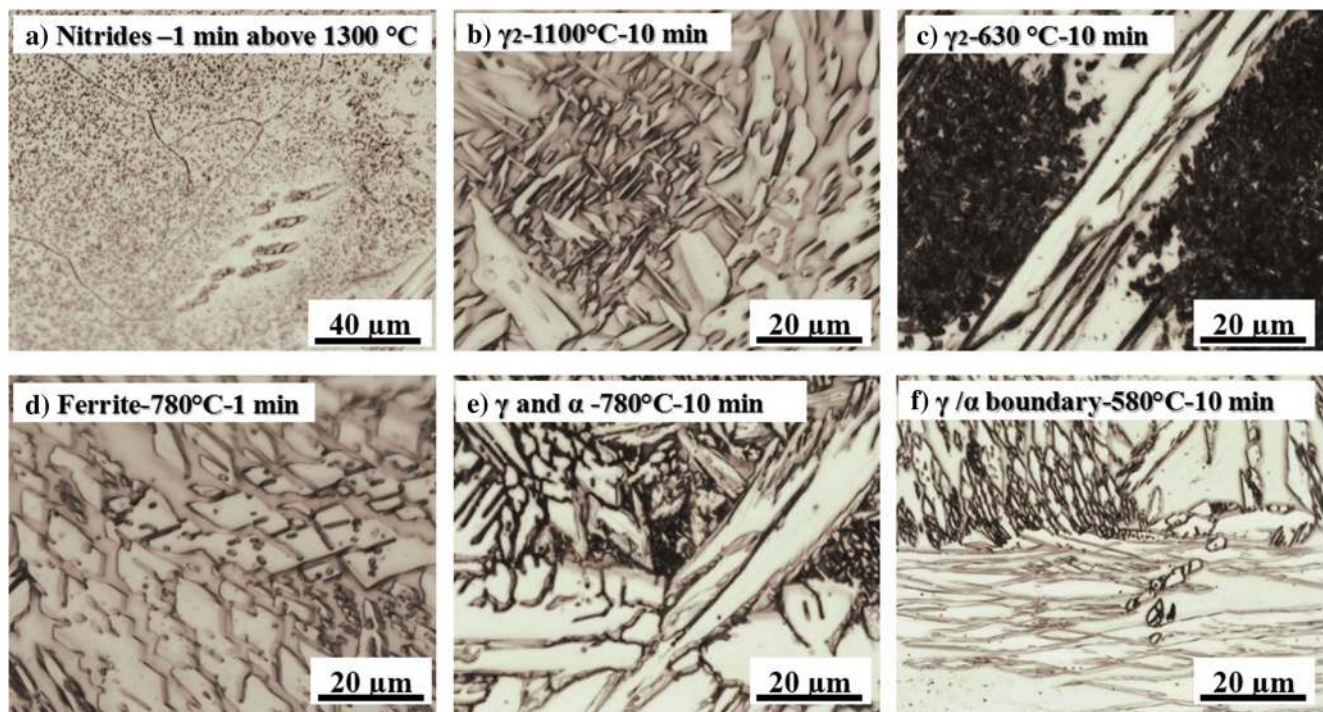
Fig. 14 Light optical micrographs of different regions in 1 and 10 min samples after sensitization testing by electrolytical etching in 10% oxalic acid. **a** Sensitization due to nitride precipitation in FBZ. **b** coarse secondary austenite did not cause significant sensitization, but **c** fine intragranular secondary austenite was sensitized. **d** Sensitization in narrow ferrite arms were seen at 780 °C, **e** greater sensitization in 10 min sample at 780 °C, and **f** sensitization of ferrite/austenite phase boundaries

temperatures (Fig. 15), form due to slower diffusion and easier nucleation due to the larger thermodynamical driving force. At higher temperature where nucleation is limited, growth is the prominent mechanism and therefore coarser secondary austenite form. The morphology of secondary austenite observed in this study is in good agreement with that reported for weld metals in other studies [10, 22–24].

Austenite may also form through the eutectoid transformation of ferrite to sigma phase and austenite. However, in real welding thermal cycles or short heat treatment times, as the 1-min heat treatment, this type of austenite may be not observed.

4.3.2 Sigma phase

As shown in Fig. 12, the most rapid precipitation of sigma phase occurs between 750 and 900 °C, where 1% sigma phase formed in less than 1 min and with a maximum after 1 min of 3.2% at 780 °C. This can be compared to results of Nilsson et al. [11] who reported precipitation of 1% intermetallics at around 780–1000 °C after 1 min in a SDSS weld metal. Different precipitation kinetics might be the result of different initial ferrite/austenite ratios, chemical compositions, and heating rates to the holding temperature. Furthermore, the nose of the precipitation curve in the TTP diagram predicted by JMatPro (Fig. 5) is located at least 100 °C higher compared to the present results. A likely reason is that JMatPro does not consider the initial weld metal non-equilibrium distribution of alloying elements, which is expected to have a significant influence on the precipitation behavior [25].

Blocky and coral-shaped sigma phase, as shown in Fig. 15, have also been reported by Martins et al. [26] for a cast duplex stainless steel. Figure 10 demonstrates that sigma is mainly present as discrete blocky particles

in ferrite/austenite boundary after 1 min at 780 °C but changes to coral shaped after 10 min. The morphology has been attributed to a higher number of nuclei at lower temperatures in other studies. However, the present study suggests that growth also plays an important role, presumably as an effect of the required diffusion which obviously is affected by the temperature.

4.3.3 Chi phase

Chi precipitated as discrete particles in small amounts at temperatures above 750 °C (Table 2 and Fig. 11). As amounts were much smaller than for sigma, it is not likely that the chi precipitates, themselves, have any major effect on properties for these heat treatment temperatures. However, at lower temperatures, thin chi phase films (Fig. 12), previously also observed by Karlsson et al. [27] in a 2205 DSS weld metal, could be more detrimental as they decorated many ferrite/austenite phase boundaries and as the sigma content was smaller. It has been proposed that chi phase can also act as a nucleation site for sigma, which indirectly increases their negative influence on properties [4].

4.3.4 Nitrides

The precipitation of nitrides in the FBZ (corresponding to HTHAZ in welds) is schematically shown in Fig. 15. Precipitation in highly ferritic regions, on cooling to room temperature in the HTHAZ, is a well-known phenomenon reported in literature [28–33]. Higher peak temperatures followed by rapid cooling to temperatures where nitrides are stable increase the nitride content. This is due to that this restricts austenite formation and
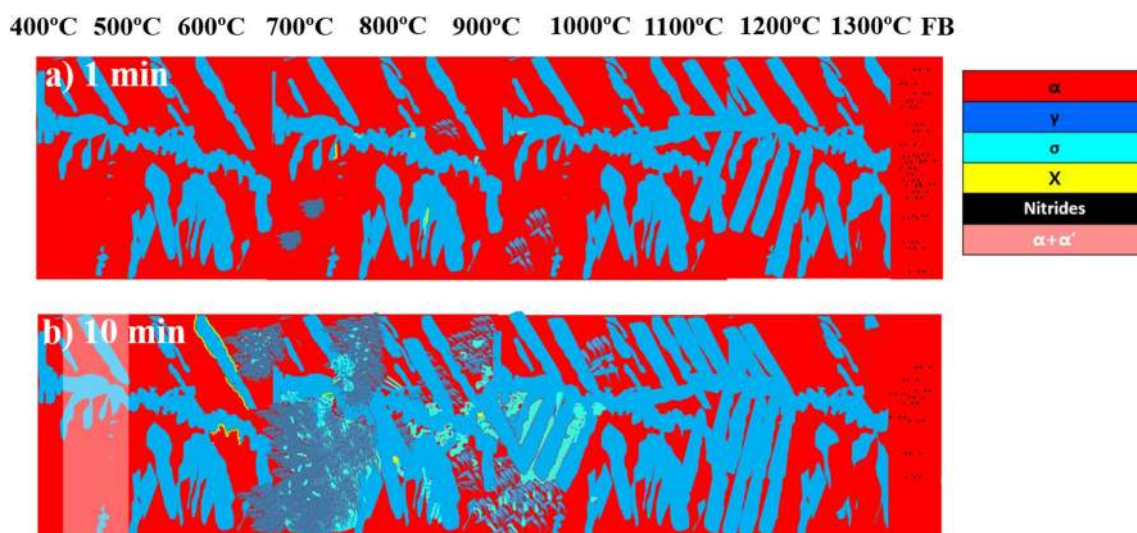
Fig. 15 Schematic illustrations of microstructure of weld metal after **a**) 1- and **b** 10-min arc heat treatment. Significant amounts of secondary austenite and sigma phase, together with some chi phase, had precipitated after 10-min arc heat treatment

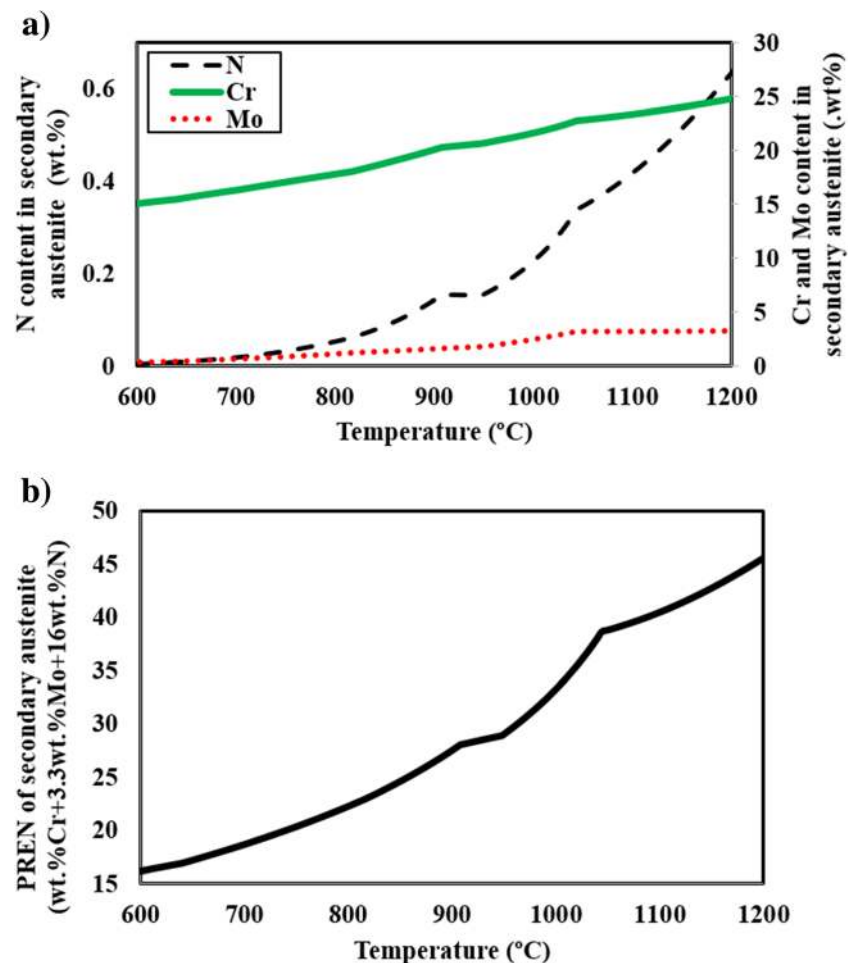**Table 3** Chemical composition (wt.%) of ferrite in the remelted region

	Si	Mn	Cr	Ni	Mo	N	W	C+P+S+Cu	Fe
Ferrite	0.45	0.55	26.59	7.58	4.52	0.08	0.05	< 0.2 wt.%,	Bal.

causes super saturation of nitrogen in ferrite, which promotes the precipitation of nitrides. The lower content of nitrides in the HTHAZ after 10 min, compared to after 1 min, is probably the result of nitrogen loss.

4.3.5 Other phases

Minor amounts of other phases such as Pi nitride, R, which has earlier been observed in 2205 weld metal [27], G, carbides, and Laves phase, all predicted to form by JMatPro (Fig. 6), might possibly also be present in the 10 min sample. However, more detailed microstructural studies with for example transmission electron microscopy would be required to identify these.

4.4 Properties

4.4.1 Hardness

Sigma phase There is a clear correlation between hardness and the sigma phase content. The precipitation of 3.2% sigma phase after 1 min, only slightly increased the hardness, as shown in Fig. 13. After 10 min, regions treated in the temperature range of 700–920 °C shows the maximum hardness, which is where the highest content of sigma phase was observed. However, hardness is not a good indicator for the loss of mechanical properties, as the impact toughness has been reported to drop significantly also for 3% sigma phase [30].

475 °C embrittlement High hardness and a low contrast etching response occurred after 10 min in regions heat treated around 475 °C which is the temperature regime where JMatPro predicted formation of Cr-rich and Fe-rich ferrite. Nilsson et al. [34] heat-treated 22Cr–3Mo–8Ni weld metal and reported that spinodal decomposition of ferrite caused embrittlement accompanied by a hardness increase at the same temperature. Örnek et al. [35] used Volta potential testing and

Fig. 16 Thermodynamic calculations of secondary austenite precipitation. **a** Content of N, Mo, and Cr in secondary austenite forming in ferrite with a composition corresponding that calculated at equilibrium at 1250 °C. **b** PREN of secondary austenite forming at different temperature

verified that ferrite decomposition reduced the Volta potential difference between ferrite and austenite in type 2205 DSS resulting in a similar etching behavior of the two phases. Therefore, the etching response and hardness increase together are strong indications of ferrite decomposition, so-called 475 °C embrittlement, occurring in the weld metal in the 10 min sample.

4.4.2 Sensitization behavior

Nitrides (in the FBZ), early-stage sigma phase (in 1 min sample), and chi phase precipitation at phase boundaries resulted in the sensitization of the adjacent ferrite. This has earlier been proven to be due to the depletion of Cr and/or Mo [36–38]. As the longer heat treatment time in this study resulted in less nitride formation, less sensitization occurred in the FBZ in the 10 min sample. In contrast, eutectoid austenite which

formed together with coral shaped sigma phase in the 10 min sample was heavily etched during sensitization testing, presumably as a consequence of its low content of Mo, Cr, and N [39]. Overall, the longer heat treatment time led to the precipitation of more intermetallics, especially sigma phase, and hence more pronounced sensitization, which was also reported by Hertzman et al. [40].

It has been claimed that secondary austenite has better corrosion properties compared to ferrite but worse than primary austenite [41]. The present study cannot confirm this with certainty but fine secondary austenite, formed at lower temperatures, definitely etched heavily suggesting sensitization (Fig. 15). Thermodynamic calculations were performed attempting to explain this observation. It was assumed that the chemical composition of ferrite in the remelted region is similar to the equilibrium composition at 1250 °C (Table 3), at which the
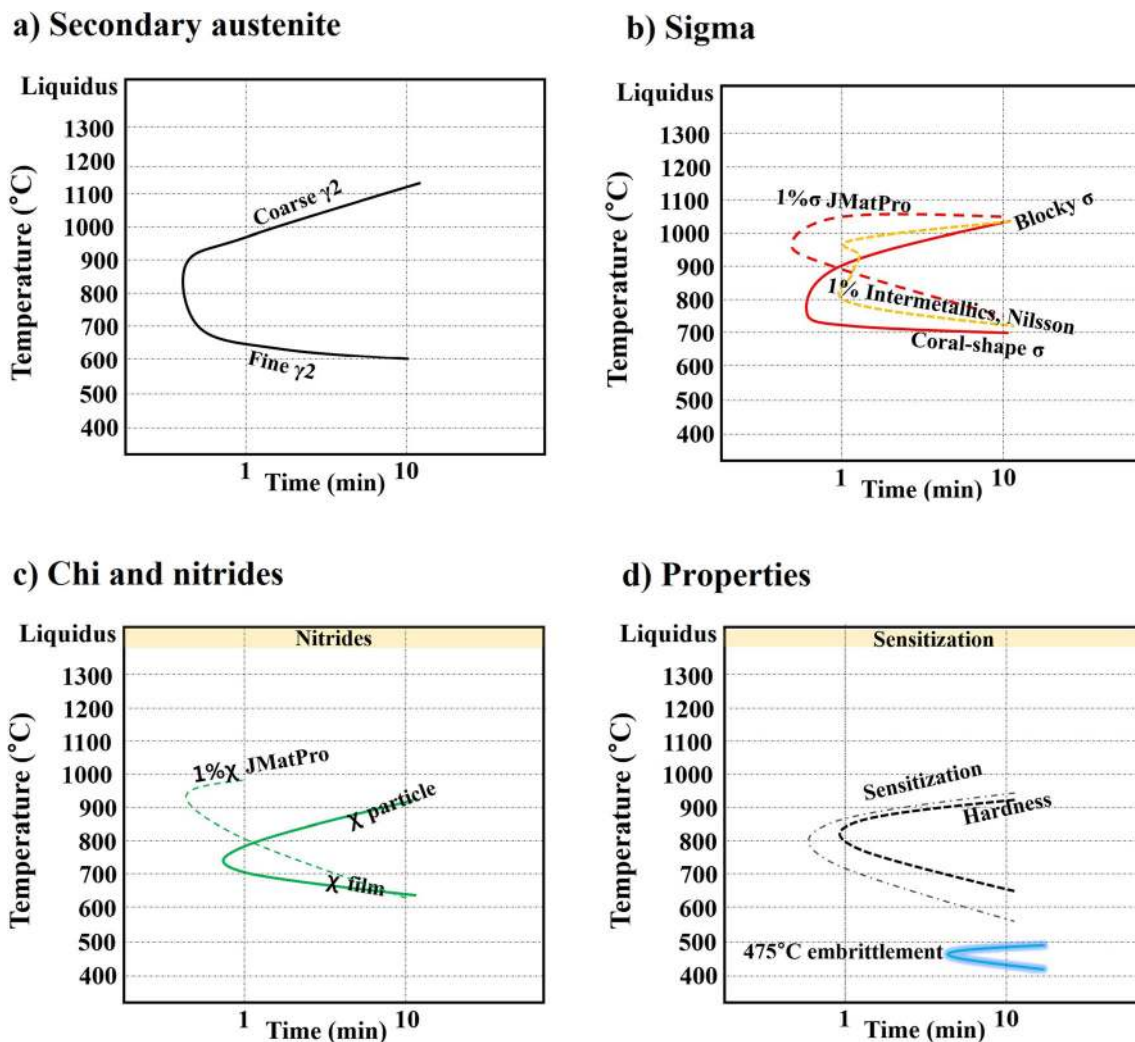
Fig. 17 Proposed TTP diagrams for type 2509 super duplex stainless steel weld metal based on observations for 1- and 10-min heat treatments. The diagrams also present information on the morphology of different phases and of sensitization and hardness above 285HV0.5 (embrittlement). **a** Secondary austenite, **b** sigma phase, **c** chi phase, and **d** sensitization and hardness (embrittlement). Hardness increase was used to predict 475 °C embrittlement. Note: nitrides precipitate in highly ferritic regions on cooling after heat treatment

equilibrium content of ferrite is about equal to its content in the remelted region before arc heat treatment.

The equilibrium composition of secondary austenite precipitating in ferrite with this composition was then calculated for different temperatures as shown in Fig. 16a. It can be noted that secondary austenite precipitating at higher temperature is richer in Cr and Mo and significantly higher in N.

The contents of these three elements are generally used to calculate pitting resistance equivalent (PREN) with the following formula:

$$PREN = wt.\%Cr + 3.3wt.\%Mo + 16wt.\%N$$

The phases with lower PREN are more susceptible to pitting attack [42]. As may be seen in Fig. 16b, the finer secondary austenite precipitating at lower temperature has much lower PREN, compared to the coarser one precipitating at higher temperature. Therefore, the observed larger sensitization of finer austenite is in agreement with that predicted by calculations.

4.5 Concluding remarks

Time-temperature-precipitation and property diagrams proposed based on the present studies of samples heat treated for 1 and 10 min are shown in Fig. 17. The nose position of curves should of course be used with caution as these could not be defined exactly based the present study. The precipitation of secondary austenite is presented in Fig. 17a. Start of sigma phase precipitation, and typical morphologies, are shown in Fig. 17b. As pointed out earlier, reasonable agreement was found with results of Nilsson et al. [11] whereas calculations with JMatPro suggests that rapid formation should occur at much higher temperature than observed. The precipitation of nitrides and chi is shown in Fig. 17c. Also for chi, there is a discrepancy between observed and predicted temperatures for most rapid formation. Time-temperature-hardness and sensitization curves are presented in Fig. 17d. The nose of the curve for 475 °C embrittlement should be used with care as no indication of increased hardness (embrittlement) was found in the 1 min sample. However, there was definitely an increase in hardness, accompanied by a change in etching response, in the 10 min sample (Fig. 14).

5 Conclusions

Microstructures, covering the complete temperature range from ambient to liquidus, were produced by arc heat treatment of as-welded 2509 type super duplex stainless steel weld metal. The evolution of microstructure, sensitization behavior, and hardness was characterized and compared to the as-welded condition, after heat treatment for 1 and 10 min.

Results are summarized as time-temperature-precipitation and property diagrams. The following was concluded:

1. Austenite content decreased above approximately 1250 °C, which promoted precipitation of nitrides in ferrite during rapid cooling. This effect was more pronounced for the longer heat treatment time.
2. The growth of primary austenite at high temperatures and the precipitation of secondary austenite at intermediate and low temperatures increased the austenite content between 600 and 1250 °C.
3. Sigma phase precipitated at 700–1020 °C, with maximum contents of 3.2% after 1 min and 18.0% after 10 min at 780 °C. Sigma typically had a blocky shape at higher temperatures and a combination of blocky and more coral-like shapes at lower temperatures.
4. Chi phase precipitated as discrete particles at 700–800 °C, but as thin films at ferrite/austenite phase boundaries at 600–700 °C.
5. Formation of sigma, chi, nitrides and fine secondary austenite caused significant sensitization. The sensitization temperature range increased from 720–840 °C after 1 min to 580–920 °C after 10 min heat treatment.
6. Sensitization due to formation of fine secondary austenite can be understood in terms of its low Cr, Mo, and N content predicted by thermodynamical calculations.
7. Formation of sigma was accompanied by an increase in hardness and was most pronounced at 700–920 °C. The increased hardness in regions heat treated around 475 °C for 10 min was interpreted as being due to ferrite decomposition, so-called 475 °C embrittlement.

References

1. Olsson J, Snis M (2007) Duplex—a new generation of stainless steels for desalination plants. Desalination 205(1):104–113. https://doi.org/10.1016/j.desal.2006.02.051

2. Olsson J (2005) Stainless steels for desalination plants. Desalination 183(1):217–225. https://doi.org/10.1016/j.desal.2005.02.050

3. Nilsson J-O (1992) Super duplex stainless steels. Mater Sci Technol 8(8):685–700. https://doi.org/10.1179/mst.1992.8.8.685

4. Nilsson J-O, Chai G (2010) The physical metallurgy of duplex stainless steels. Paper presented at the Duplex Stainless Steel Conference. Beaune, France

5. Karlsson L (1995) Welding duplex and super duplex stainless steels. Anti-Corros Methods Mater 42(6):30–35. https://doi.org/10.1108/eb007380

6. Karlsson (2012) Welding duplex stainless steels—a review of current recommendations. Weld World 56(5–6):65–76. https://doi.org/10.1007/BF03321351

7. Handbook of stainless steel (2013). Outokumpu Oyj, Finland

8. Karlsson L (2012) Welding of duplex stainless steels–a review of current recommendations. Weld World 56(5):6

9. Nishimoto K, Saida K, Katsuyama O (2006) Prediction of sigma phase precipitation in super duplex stainless steel weldments. Weld World 50(3–4):13–28. https://doi.org/10.1007/BF03263429

10. Nilsson J-O, Karlsson L, Andersson J-O (1995) Secondary austenite for mation and its relation to pitting corrosion in duplex stainless steel weld metal. Materials Sci Technol 11(3):276–283. https://doi.org/10.1179/mst.1995.11.3.276

11. Nilsson J-O, Huhtala T, Jonsson P, Karlsson L, Wilson A (1996) Structural stability of super duplex stainless weld metals and its dependence on tungsten and copper. Metall Mater Trans A 27(8): 2196–2208. https://doi.org/10.1007/BF02651874

12. Hosseini V, Hurtig K, Karlsson L (2016) Effect of multipass TIG welding on the corrosion resistance and microstructure of a super duplex stainless steel. Mater Corros 68(4):405–415

13. Hosseini VA, Bermejo MAV, Gårdstam J, Hurtig K, Karlsson L (2016) Influence of multiple thermal cycles on microstructure of heat-affected zone in TIG-welded super duplex stainless steel. Weld World 60(2):233–245. https://doi.org/10.1007/s40194-016-0300-5

14. Gregori A, Nilsson J-O (2002) Decomposition of ferrite in commercial superduplex stainless steel weld metals; microstructural transformations above 700 °C. Metall Mater Trans A 33(4):1009–1018. https://doi.org/10.1007/s11661-002-0202-6

15. Wessman S, Pettersson R (2015) Application of computational thermodynamics to predict growth of intermetallic phases in superduplex stainless steels. Steel Res Int 86(11):1339–1349. https://doi.org/10.1002/srin.201400277

16. Ferguson D, Chen W, Bonesteel T, Vosburgh J (2009) A look at physical simulation of metallurgical processes, past, present and future. Materials Sci Eng A 499(1):329–332. https://doi.org/10.1016/j.msea.2007.10.121

17. Hosseini VA, Karlsson L, Hurtig K, Choquet I, Engelberg D, Roy MJ, Kumara C (2017) A novel arc heat treatment technique for producing graded microstructures through controlled temperature gradients. Mater Des 121:11–23. https://doi.org/10.1016/j.matdes.2017.02.042

18. Brayshaw WJ, Roy MJ, Sun T, Akrivos V, Sherry AH (2016) Iterative mesh-based hardness mapping. Sci Technol Welding Joining:1–8

19. International A (2015) ASTM A262–15: standard practices for detecting susceptibility to intergranular attack in austenitic stainless steels. West Conshohocken, PA

20. Kumara C (2016) Modelling of the temperature field in TIG arc heat treated super duplex stainless steel samples. University West, Sweden

21. Roscoe CV, Gradwell KJ, Lorimer GW Structure/stability relationships in series of duplex stailess steels. In, 1986. Nederlands, pp 126–135

22. Ramkumar KD, Thiruvengatam G, Sudharsan S, Mishra D, Arivazhagan N, Sridhar R (2014) Characterization of weld strength and impact toughness in the multi-pass welding of super-duplex

23. Zhang Z, Jing H, Xu L, Han Y, Zhao L (2016) Investigation on microstructure evolution and properties of duplex stainless steel joint multi-pass welded by using different methods. Mater Des 109:670–685. https://doi.org/10.1016/j.matdes.2016.07.110

24. Kang DH, Lee HW (2012) Effect of different chromium additions on the microstructure and mechanical properties of multipass weld joint of duplex stainless steel. Metall Mater Trans A 43(12):4678–4687. https://doi.org/10.1007/s11661-012-1310-6

25. Sato YS, Kokawa H (1999) Preferential precipitation site of sigma phase in duplex stainless steel weld metal. Scr Mater 40(6):659–663. https://doi.org/10.1016/S1359-6462(98)00483-7

26. Martins M, Casteletti LC (2009) Sigma phase morphologies in cast and aged super duplex stainless steel. Mater Charact 60(8):792–795. https://doi.org/10.1016/j.matchar.2009.01.005

27. Karlsson L, Ryen L, Pak S (1995) Precipitation of intermetallic phases in 22% Cr duplex stainless weld metals. Weld J-Including Welding Res Suppl 74(1):28–38

28. Hosseini VA, Wessman S, Hurtig K, Karlsson L (2016) Nitrogen loss and effects on microstructure in multipass TIG welding of a super duplex stainless steel. Mater Des 98:88–97. https://doi.org/10.1016/j.matdes.2016.03.011

29. Chen T, Yang J (2002) Microstructural characterization of simulated heat affected zone in a nitrogen-containing 2205 duplex stainless steel. Mater Sci Eng A 338(1):166–181. https://doi.org/10.1016/S0921-5093(02)00065-5

30. Hsieh R, Liou H-Y, Pan Y-T (1999) Weldability of 22% Cr duplex stainless steels. China Steel Techn Rep (Taiwan) 13:14–26

31. Matsunaga H, Sato Y, Kokawa H, Kuwana T (1998) Effect of nitrogen on corrosion of duplex stainless steel weld metal. Sci Technol Weld Join 3(5):225–232. https://doi.org/10.1179/stw.1998.3.5.225

32. Ramirez A, Brandi S, Lippold J (2004) Secondary austenite and chromium nitride precipitation in simulated heat affected zones of duplex stainless steels. Sci Technol Weld Join 9(4):301–313. https://doi.org/10.1179/136217104225021715

33. Hertzman S, Brolund B, Ferreira PJ (1997) An experimental and theoretical study of heat-affected zone austenite reformation in three duplex stainless steels. Metall Mater Trans A 28(2):277–285. https://doi.org/10.1007/s11661-997-0130-6

34. Nilsson J-O, Liu P (1991) Aging at 400–600 C of submerged arc welds of 22Cr–3Mo–8Ni duplex stainless steel and its effect on toughness and microstructure. Mater Sci Technol 7(9):853–862. https://doi.org/10.1179/mst.1991.7.9.853

35. Örnek C, Walton J, Hashimoto T, Ladwein T, Lyon S, Engelberg D (2017) Characterization of 475° C embrittlement of duplex stainless steel microstructure via scanning kelvin probe force microscopy and magnetic force microscopy. J Electrochem Soc 164(6):C207–C217. https://doi.org/10.1149/2.0311706jes

36. Tan H, Wang Z, Jiang Y, Han D, Hong J, Chen L, Jiang L, Li J (2011) Annealing temperature effect on the pitting corrosion resistance of plasma arc welded joints of duplex stainless steel UNS S32304 in 1.0 M NaCl. Corros Sci 53(6):2191–2200. https://doi.org/10.1016/j.corsci.2011.02.041

37. Pohl M, Storz O, Glogowski T (2007) Effect of intermetallic precipitations on the properties of duplex stainless steel. Mater Charact 58(1):65–71. https://doi.org/10.1016/j.matchar.2006.03.015

38. Kim S-T, Lee I-S, Kim J-S, Jang S-H, Park Y-S, Kim K-T, Kim Y-S (2012) Investigation of the localized corrosion associated with phase transformation of tube-to-tube sheet welds of hyper duplex stainless steel in acidified chloride environments. Corros Sci 64: 164–173. https://doi.org/10.1016/j.corsci.2012.07.014

stainless steel UNS 32750. Mater Des 60:125–135. https://doi.org/10.1016/j.matdes.2014.03.031

39. de Méloa EB, Magnaboscob R, de Moura Netoa C (2013) Influence of the Microstructure on the Degree of Sensitization of a Duplex Stainless Steel UNS S31803 Aged at 650 C. Mater Res 16(6):1336–1343

40. Hertzman S, Huhtala T, Karlsson L, Nilsson J-O, Nilsson M, Jargelius-Pettersson R, Wilson A (1997) Microstructure–property relations of Mo-and W-alloyed super duplex stainless weld metals. Mater sci Technol 13(7):604–613. https://doi.org/10.1179/mst.1997.13.7.604

41. Muthupandi V, Bala Srinivasan P, Seshadri SK, Sundaresan S (2003) Effect of weld metal chemistry and heat input on the structure and properties of duplex stainless steel welds. Mater Sci Eng A 358(1–2):9–16. https://doi.org/10.1016/S0921-5093(03)00077-7

42. Tan H, Jiang Y, Deng B, Sun T, Xu J, Li J (2009) Effect of annealing temperature on the pitting corrosion resistance of super duplex stainless steel UNS S32750. Mater Charact 60(9):1049–1054. https://doi.org/10.1016/j.matchar.2009.04.009